



RESEARCH ARTICLE

Thermal and angular dependence of next-generation photovoltaics under indoor lighting

Chia-Yuan Chen¹ | Ting-Yang Kuo² | Chien-Wu Huang¹ | Zih-Hong Jian¹ | Po-Tsung Hsiao³ | Chin-Li Wang^{4,5} | Jian-Ci Lin⁶ | Chien-Yu Chen⁷ | Chao-Hsuan Chen⁸ | Yung-Liang Tung³ | Ming-Chi Tsai⁴ | Kuan-Min Huang⁸ | Chih-Ming Chen⁹ | Cheng-Wei Hsu⁵ | Yen-Chiao Chen⁹ | Zingway Pei¹⁰ | Yogesh S. Tingare¹¹ | Hsien-Hsin Chou¹¹ | Chen-Yu Yeh¹¹ | Ching-Yao Lin⁴ | Yuh-Lang Lee⁶ | Hao-Wu Lin⁷ | Hsin-Fei Meng¹² | Pi-Tai Chou² | Chun-Guey Wu¹

¹ Research Center of New Generation Light Driven Photovoltaic Modules and Department of Chemistry, National Central University, Zhong-Li 32001 Taiwan, Republic of China

² Department of Chemistry, National Taiwan University, Taipei 10617 Taiwan, Republic of China

³ Green Energy and Environment Research Laboratories, Industrial Technology Research Institute, Hsinchu 31040 Taiwan, Republic of China

⁴ Department of Applied Chemistry, National Chi Nan University, Nantou 54561 Taiwan, Republic of China

⁵ Taiwan DSC PV Ltd., Taoyuan 32844 Taiwan, Republic of China

⁶ Department of Chemical Engineering, National Cheng Kung University, Tainan 70101 Taiwan, Republic of China

⁷ Department of Materials Science and Engineering, National Tsing Hua University, Hsinchu 30013 Taiwan, Republic of China

⁸ Department of Photonics and Institute of Electro-Optical Engineering, College of Electrical and Computer Engineering, National Chiao Tung University, Hsinchu 30078 Taiwan, Republic of China

⁹ Department of Chemical Engineering, National Chung Hsing University, Taichung 402 Taiwan, Republic of China

¹⁰ Graduate Institute of Optoelectronic Engineering, National Chung Hsing University, Taichung 402 Taiwan, Republic of China

¹¹ Department of Chemistry, Research Center for Sustainable Energy and Nano-technology (RCSEN), and Innovation and Development Center of Sustainable Agriculture (IDCSA), National Chung Hsing University, Taichung 402 Taiwan, Republic of China

¹² Institute of Physics, National Chiao Tung University, Hsinchu 30078 Taiwan, Republic of China

Correspondence

Chia-Yuan Chen, Research Center of New Generation Light Driven Photovoltaic Modules and Department of Chemistry, National Central University, Zhong-Li 32001, Taiwan, Republic of China.

Email: chiayuan@ncu.edu.tw

Chen-Yu Yeh, Department of Chemistry, Research Center for Sustainable Energy and Nano-technology (RCSEN), and Innovation and Development Center of Sustainable Agriculture (IDCSA), National Chung Hsing University, Taichung 402, Taiwan, Republic of China.

Email: cyeh@dragon.nchu.edu.tw

Ching-Yao Lin, Department of Applied Chemistry, National Chi Nan University, Nantou 54561, Taiwan, Republic of China. Email: cylv@ncnu.edu.tw

Yuh-Lang Lee, Department of Chemical Engineering, National Cheng Kung University, Tainan 70101, Taiwan, Republic of China.

Abstract

Next-generation photovoltaic technologies such as dye-sensitized solar cells, organic thin-film photovoltaics and perovskite solar cells are promising to efficiently harvest ambient light energy. However, more and deeper understanding of their photovoltaic characteristics is essential to create new applications under room light illumination. In this study, for the first time, the difference in temperature coefficients and angular dependence of photovoltaic parameters for the large-area devices are investigated systematically under the compact fluorescent lamp and light-emitting diode light. These emerging photovoltaic devices, compared with the single crystalline silicon solar cells, not only have higher open-circuit voltage (up to approximate 1 V) and better power conversion efficiency (in the range of 9.2% ~ 22.6%) but also exhibit less temperature dependent voltage and output power ($< -0.6\% \text{ } ^\circ\text{C}^{-1}$), as well as broader angular response (over 75 degrees). The state-of-the-art dye-sensitized and organic thin-film devices also show advantageously positive temperature coefficients of current, and the latter even has positive thermal dependence of fill factor. These features

Email: ylee@mail.ncku.edu.tw

Hao-Wu Lin, Department of Materials Science and Engineering, National Tsing Hua University, Hsinchu 30013, Taiwan, Republic of China.

Email: hwlin@mx.nthu.edu.tw

Hsin-Fei Meng, Institute of Physics, National Chiao Tung University, Hsinchu 30078, Taiwan, Republic of China.

Email: meng@mail.nctu.edu.tw

Pi-Tai Chou, Department of Chemistry, National Taiwan University, Taipei 10617, Taiwan, Republic of China.

Email: chop@ntu.edu.tw

Chun-Guey Wu, Research Center of New Generation Light Driven Photovoltaic Modules and Department of Chemistry, National Central University, Zhong-Li 32001, Taiwan, Republic of China.

Email: t610002@cc.ncu.edu.tw

Funding information

Ministry of Science and Technology (MOST), Taiwan, Republic of China, Grant/Award Numbers: 107-2113-M-008-016-MY2, 105-2119-M-009-008, 105-2628-E-007-008-MY3, 105-2112-M-007-016-MY3, 106-2119-M-006-003, 106-2119-M-260-001, 106-2119-M-005-001, 106-2731-M-008-001, 106-2119-M-008-022 and 106-2731-M-008-003-MY2

suggest the next-generation photovoltaic devices are more favorable than the conventional crystalline silicon solar cells for real-life indoor applications.

KEYWORDS

dye-sensitized solar cells, organic thin-film photovoltaics, perovskite solar cells, indoor lighting, temperature and angular dependent power

1 | INTRODUCTION

Electricity nowadays is an essential element of modern life and will be increasing in high demand in the near future. Amongst the renewable energy technologies, photovoltaic (PV) solar cells are currently the best choice to indoor applications, in particular, to power electronic devices under room lighting for the Internet of Things (IoT).¹⁻³ The next-generation PV technologies such as dye-sensitized solar cells (DSCs),⁴⁻¹³ organic thin-film photovoltaics (OPVs),¹⁴⁻²⁰ and perovskite solar cells (PSCs)²¹⁻²⁴ have attracted recently great attention because of their high potential in both outdoor and indoor applications. It has been noted that their spectral responsivity mainly covers the visible domain due to the energy gap of light harvesting materials, which promises an efficient conversion of indoor light into electricity. Furthermore the cost effectiveness, flexibility and colorfulness of the devices are the desirable features for driving wireless sensors, signal transmitters and portable electronics under ambient light. The modern lighting sources, for example, the compact fluorescent lamps (CFL) and light-emitting diodes (LED) used in indoor environments (such as rooms, offices and warehouses) offer illuminance in the range of 200 lx ~ 1000 lx.¹⁵ The corresponding irradiance could be higher than sub-milliwatt per square centimeter. Once a portion of the light energy can be captured by highly efficient PVs, the output power will be satisfactory to trigger automatically the up-to-date sensing nodes for the IoT.

It was reported that the DSCs and PSCs under the CFL with illuminance of 1000 lx have achieved high power conversion efficiency

(PCE) up to 28.9% and 27.4%, respectively.^{10,22} Under the same illumination level, an OPV having PCE of ca. 13% to power the wireless sensors has been demonstrated.²⁰ Despite the PCE landmarks, the thermal and angular dependence of the emerging PVs under indoor light conditions have never been systematically studied so far, which are required urgently to bring the next-generation PVs into daily life. In this study the performance of five state-of-the-art PV devices [three DSCs sensitized respectively with TY6,¹¹ AN-11,¹³ and N719 dye,²⁵ an inverted (p-i-n structure) PSC based on methylammonium lead iodide (MAPbI₃) absorber,²⁶ and an OPV using PTB7-Th:PC₇₁BM as an active layer²⁷] were investigated systematically. The full names and structures of major light-harvesting materials applied in the cells are provided in Supporting Information and Figure 1, respectively. To approach actual indoor utilizations, the area of three DSCs and OPV-PTB7-Th devices confined with a black aluminum mask having an aperture area of 5 × 1 cm², while the PSC-MAPbI₃ cell has the aperture area of 2 × 2 cm² due to convenience of depositing uniformly the materials. The photos of the devices are displayed in Figure S1 (Supporting Information). Based on their highest efficiency and best stability (compared with other cells belong to the same PV category), the "top 5" large-area devices were selected from 42 samples (including 12 DSCs, 15 PSCs and 15 OPVs) submitted by thirteen new-generation light-driven photovoltaics research teams involved in a joint program funded by the Ministry of Science and Technology (MOST), Taiwan. For the first time the PV performance of these large-area devices was characterized under various indoor lighting

conditions (different lighting sources, temperature and incident angles). All the measurements of the devices were carried out at the Photovoltaic Efficiency Verification Laboratory (PVEVL) of National Central University (NCU), Taiwan, which has been accredited on the basis of the ISO/IEC 17025.

2 | EXPERIMENTAL

2.1 | Device fabrication and packing

The materials and fabrication of devices were provided in Supporting Information. After sealing the devices, two leads were attached to each sample as terminals to assure a secure four-wire connection and to improve the repeatability of performance characterization.²⁸ Moreover, the mask was attached successively onto the samples to confine the area of devices and diminish the undesired light reflection and diffusion.

2.2 | PV performance characterization of devices

The CFL lighting system based on the Philips TL5 Essential 14W/865 tubes was homemade. Another lighting system using the Osram LED lamps (Star CLA75 865) was manufactured by the Yamashita Denso Corporation (YILS-P150), Japan. Both the lighting sources have color temperature of 6500 K. The absolute illuminance (1000 lx) and the illumination non-uniformity of lighting systems were adjusted then measured using an illuminance meter (T10A) calibrated by the JEMIC, Japan (certificate No. 011-158653-A00). A spectroradiometer (HSSR-1300) calibrated with a spectral irradiance standard lamp (certificate No. CC43-0074-0, traceable to the NMIJ, Japan) was applied to obtain

the spectral irradiance of the lighting systems. After measuring the illuminance, non-uniformity and spectral irradiance of light sources, the device under test was mounted on a temperature and angle (θ ; from 0 degree (normal incidence) to 90 degrees) controllable stage (PVC-2070). The current-voltage (I - V) source measure unit (ADCMT 6244) and temperature monitor (Agilent 34972A connected with a T-type thermocouple) were used in the performance characterization of devices under various conditions, which all have the calibrations traceable to the NML, Taiwan (certificate No. 16-08-BAC-605-04L and 18-07-BAC-077-05L, respectively). In addition to the emerging PVs, for a fair comparison, a commercial single crystalline silicon solar reference cell (c-Si; model AK-200 from the Konica Minolta, Japan) was also measured under the same conditions. The I - V measurements of the devices were divided into three parts: (1) under illumination of different sources, CFL and LED (1000 lx), (2) under various device temperature, and (3) under different incident angles. In the first section of measurements, the current hysteresis for the devices was investigated initially under the CFL light (ca. 1000 lx) with various I - V sampling delay time (from 10 ms to 15 s) and different sweeping directions, in which the forward mode was scanning from I_{sc} (short-circuit current) to V_{oc} (open-circuit voltage) and the reverse way was from V_{oc} to I_{sc} . According to the results presented in Figure S2, the sampling delay time was selected for each device to mitigate the hysteresis (15 s for DSC-TY6, 10 s for DSC-AN-11, DSC-N719 and PSC-MAPbI₃, and 100 ms for OPV-PTB7-Th, respectively). For measuring the thermal and angular response of the devices (the second and third parts) under continuous illumination of the indoor lighting (as the I - V curves presented in Figure S3 and Figure S4, respectively), the sampling delay time of 5 s (for the DSCs and PSC-MAPbI₃) and 100 ms (for OPV-PTB7-Th) was used respectively with the forward direction of I - V sweeping to reduce the measurement time. After the I - V curves, the

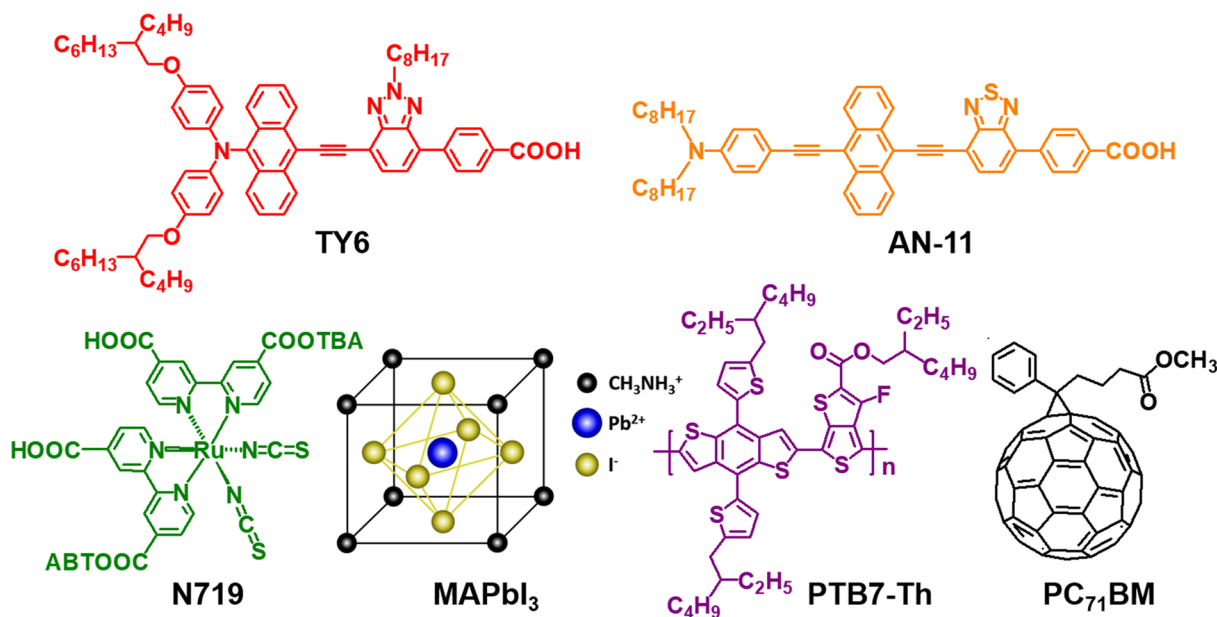


FIGURE 1 Structures of TY6, AN-11, N719, MAPbI₃ (CH₃NH₃PbI₃), PTB7-Th and PC₇₁BM for device DSC-TY6, DSC-AN-11, DSC-N719, PSC-MAPbI₃, and OPV-PTB7-Th, respectively. The TBA group in N719 denotes tetrabutylammonium. [Colour figure can be viewed at wileyonlinelibrary.com]

aperture area of shielding mask for each device was measured with an optical microscope equipped with a CCD camera (MF-UB3017B; the NML-traceable calibration certificate No. L-IR-105-08-404). All the *I*-*V* and area measurements of the devices were repeated for three times. For the first part of measurement (under an absolute illuminance of 1000 lx and the device temperature of 25 ± 1 °C), the expanded measurement uncertainty (coverage factor (*k*) of 2 for approximate 95% of confidence level) of the PV parameters was estimated, including *J*_{sc} (short-circuit current density), *V*_{oc}, FF (fill factor), MPD (maximum output power density), and PCE (calculated with Equation (1) in which *A* stands for the aperture area of sample, and *P*_{in} is the incident power of the CFL and LED light (1000 lx) as $325.21 \mu\text{W cm}^{-2}$ and $338.19 \mu\text{W cm}^{-2}$, respectively).

$$\begin{aligned} \text{PCE (\%)} &= \frac{J_{sc} (\mu\text{A}) \times V_{oc} (\text{V}) \times \text{FF (\%)} }{A (\text{cm}^2) \times P_{in} (\mu\text{W cm}^{-2})} \\ &= \frac{\text{MPD} (\mu\text{W cm}^{-2})}{P_{in} (\mu\text{W cm}^{-2})} \times 100\% \end{aligned} \quad (1)$$

For the second and third parts of measurements, the mean values and the standard deviation were included in the results. All the calibration certificates of equipment are available in Supporting Information.

3 | RESULTS AND DISCUSSION

The normalized external quantum efficiency (EQE) spectra of the five devices measured with the direct current (DC) mode²⁸ to approach the indoor operating conditions are displayed in Figure 2. The output spectra of the CFL and the LED lighting sources used in this study are also shown in Figure 2. Using an illuminometer as a prime standard in combination with a spectroradiometer,²⁹ the illuminance and spectral irradiance of the room light sources can be precisely measured. Also, the setup of photometric and radiometric meters renders an advantage that the corresponding total irradiance of the CFL and LED light can be acquired and correlated with the illuminance. The EQE profiles of the devices, except DSC-TY6, are capable of covering entirely the wavelength range of the CFL and LED lighting sources. The short-circuit current density index (*J*_{sc}^{index}) can be calculated with Equation (2) to make a fair comparison on the light harvesting capability for each device under the two artificial lighting (CFL versus LED):

$$J_{sc}^{\text{index}} = \frac{\int_{\lambda_1}^{\lambda_2} S_R(\lambda) \times E_{LED}(\lambda) d\lambda}{\int_{\lambda_1}^{\lambda_2} S_R(\lambda) \times E_{CFL}(\lambda) d\lambda} \quad (2)$$

where *S_R* (*λ*) presents the spectral responsivity of the device under test, which can be converted from the EQE spectrum [*S_R* (*λ*) = EQE (*λ*) × *λ* (nm) / 1240 (eV nm)]. *E*_{CFL} (*λ*) and *E*_{LED} (*λ*) stand for the spectral irradiance of the lighting sources. The wavelength limits (*λ*₁ and *λ*₂) encompass 380 ~ 780 nm according to the wavelength terminals defined in the CIE photopic curve (*V* (*λ*)).³⁰

The calculated *J*_{sc}^{index} values presented in Table 1 indicate DSC-TY6 harvests the CFL photons more efficiently than it captures the LED light. Conversely DSC-AN-11, DSC-N719, PSC-MAPbI₃ and

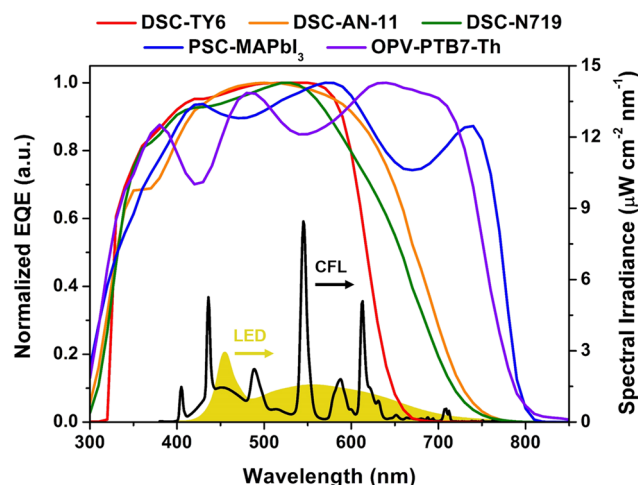


FIGURE 2 Normalized EQE spectra of devices (25 ± 1 °C) under test and spectral irradiance of CFL and LED light with an absolute illuminance adjusted to 1000 lx. [Colour figure can be viewed at wileyonlinelibrary.com]

OPV-PTB7-Th are capable of converting more LED photons into current. These results demonstrate high adaptability of these next-generation PVs in the practical indoor applications because the light harvesting materials embedded in devices can be changed easily to match the great diversity of commercially available lighting sources.

It has been reported that the hysteresis in *I*-*V* curves of DSCs and some PSCs under low intensity of illumination would be affected seriously by the sampling rate and sweeping direction.^{29,31} The comparative PV parameters summarized in Figure S2 show that all the three DSC samples exhibit the apparent capacitance effects when an inadequate sampling delay time (shorter than 1 s) is adopted. The relative FF and *P*_{max} (maximum output power) presented in Figure S2c and S2d reveal clearly that the hysteresis in DSC-TY6 is more serious than that of DSC-AN-11 and DSC-N719. The difference in current hysteresis could be ascribed to the fact that the mesoscopic TiO₂ film (16 μm) in DSC-TY6 is thicker than that of the other two DSCs (both 12 μm), resulting in a longer period of equilibrium time required for charge and ion diffusions under bias. On the other hand, the hysteretic behavior in PSC-MAPbI₃ and OPV-PTB7-Th under identical conditions is negligible, exhibiting a balanced thermodynamic diffusion of charge carriers.

Figure 3 presents the current density-voltage (*J*-*V*) curves of the devices measured respectively under the CFL and LED light (1000 lx) with an appropriate sampling delay time to alleviate the hysteresis. The corresponding PV parameters are summarized in Table 2, including these of the c-Si cell. DSC-TY6 under the CFL shows *J*_{sc} of $89.51 \mu\text{A cm}^{-2}$ which is higher than that under the LED ($84.96 \mu\text{A cm}^{-2}$). A reverse trend of *J*_{sc} is found in the other four devices, in particular, OPV-PTB7-Th ($83.84 \mu\text{A cm}^{-2}$ (CFL) versus $91.75 \mu\text{A cm}^{-2}$ (LED)). In fact, this scenario is predictable from the viewpoint of *J*_{sc}^{index}. The deviation between the measured and calculated *J*_{sc}^{index} values is less than $\pm 1.0\%$ (see Table 1), which supports the precision of the measurement protocol presented here for the first time. The five emerging PV devices exhibit *V*_{oc} (> 0.68 V) significantly higher

TABLE 1 Calculated and measured J_{sc}^{index} for devices under the two indoor lighting (CFL versus LED).

Device	DSC-TY6	DSC-AN-11	DSC-N719	PSC-MAPbI ₃	OPV-PTB7-Th
Calculated J_{sc}^{index} (LED/CFL) ^a	0.958	1.025	1.006	1.059	1.103
Measured J_{sc}^{index} (LED/CFL) ^b	0.949	1.026	1.003	1.052	1.094
Deviation in J_{sc}^{index} (%) ^c	-0.9	0.1	-0.3	-0.7	-0.9

^aThe values were obtained using Equation (2).^bThe data were extracted from the J - V curves of devices (Figure 3).^cThe results were estimated from $[(\text{measured } J_{sc}^{index} - \text{calculated } J_{sc}^{index}) \times 100\%]$.

than that of c-Si reference (ca. 0.44 V), especially Voc of ca. 1 V for DSC-AN-11 that consists of two serial-connected subcells. Among the devices, PSC-MAPbI₃ measured under the CFL and LED light achieves the highest MPD of 72.50 $\mu\text{W cm}^{-2}$ (corresponding to an estimated PCE of 22.3%) and of 76.54 $\mu\text{W cm}^{-2}$ (PCE = 22.6%), respectively. Under the same conditions, MPD of DSC-TY6, DSC-N719 and OPV-PTB7-Th ranging from 38.81 $\mu\text{W cm}^{-2}$ (PCE = 11.9%) to 53.72 $\mu\text{W cm}^{-2}$ (PCE = 16.5%) also outperforms that of c-Si cell (< 38.62 $\mu\text{W cm}^{-2}$ and PCE < 11.4%). It is worth mentioning that the Pmax of these next-generation PVs (> 149 μW) and the corresponding voltage (Vmax; > 0.56 V) is sufficient to drive autonomously the smart image sensors and radio frequency identification (RFID) tags.^{1,19}

The performance of PV devices under illumination of any light source is affected by the sample temperature, in particular, Voc and Pmax which are both critical toward real-life applications. Under simulated or natural sunlight, the influencing parameters can be summarized to the thermal expansion and contraction of materials, shifts of energy gaps and quasi-Fermi levels, different degrees of ion diffusion

(or migration), kinetic competitions between charge transfer and recombination, or variations in series resistance (R_s) and shunt resistance (R_{sh}).³²⁻⁴⁸ Accordingly, the standard testing conditions (STC) established for rating all the terrestrial photovoltaics include the device temperature of 25 °C as one of the criteria. For practical indoor applications, temperature effects on the PV parameters are extremely important because the ambient temperature is not always fixed at 25 °C. Any thermal-induced drift of the output current, voltage and power could idle or damage electronically sensitive components triggered by PV devices. Furthermore, the temperature dependence of device performance might vary due to diverse materials.²⁹ Therefore the temperature of the devices under test was switched between 15 °C and 35 °C to embrace the normal room conditions. The relative variations in PV parameters obtained under the CFL and LED light (ca. 1000 lx) are presented in Figure 4 and Figure S5, respectively. The corresponding temperature coefficients (also relative values) extracted from the slope of the fitting lines in the two figures are summarized in Table 3 to quantify the thermal effects on device performance, including α_{rel} , β_{rel} , κ_{rel} and γ_{rel} for I_{sc} , Voc, FF and Pmax, respectively.

Figure 4a clearly shows that I_{sc} of DSC-TY6 and DSC-AN-11 under the CFL enhances linearly with temperature (as the positive current-temperature coefficients (α_{rel}) presented in Table 3). Furthermore the α_{rel} value of DSC-TY6 (ca. 0.16% °C⁻¹) is remarkably higher than other devices, which renders DSC-TY6 advantages in application under the CFL light. The R_s of the three DSCs calculated from the I - V curves displays that higher temperature contributes to lower R_s (see Figure S6a). These results reveal that the magnification of I_{sc} in DSC-TY6 and DSC-AN-11 should be ascribed to the improved ionic conductivity of the electrolyte upon raising temperature. Interestingly, the temperature dependence of I_{sc} for DSC-N719 under CFL and LED light (ca. -0.02% °C⁻¹ of the α_{rel} value) is opposite to that of the former two DSC devices even though the thermal-induced variation in R_s is similar. The temperature dependence of R_{sh} for the devices (Figure S6c) is scrutinized to solve the puzzle. It is found that R_{sh} of DSC-N719 decreases at higher temperature, which is different from the trend observed in both DSC-TY6 and DSC-AN-11. The results may indicate that the facile ion diffusion in the printable electrolyte having PEO and PMMA for DSC-N719 causes more undesired charge recombination at higher temperature and hence reduces the output current.

The negative α_{rel} value (ca. -0.02% °C⁻¹) of PSC-MAPbI₃ under the CFL and LED light is comparable with that of DSC-N719 and c-Si (Table 3). Although the temperature dependence of R_s and R_{sh}

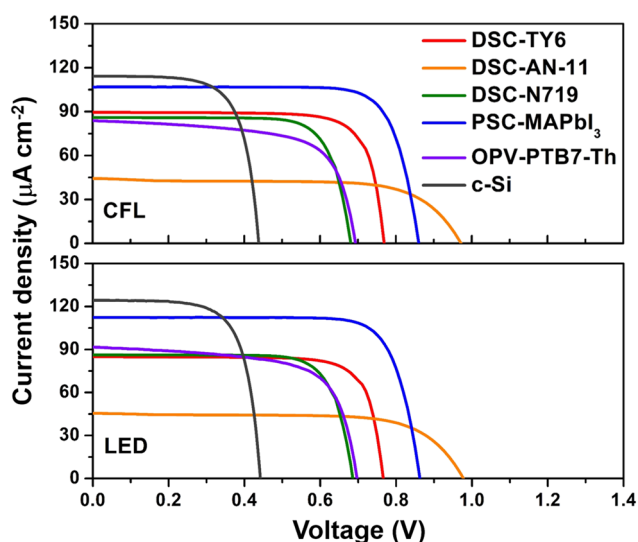
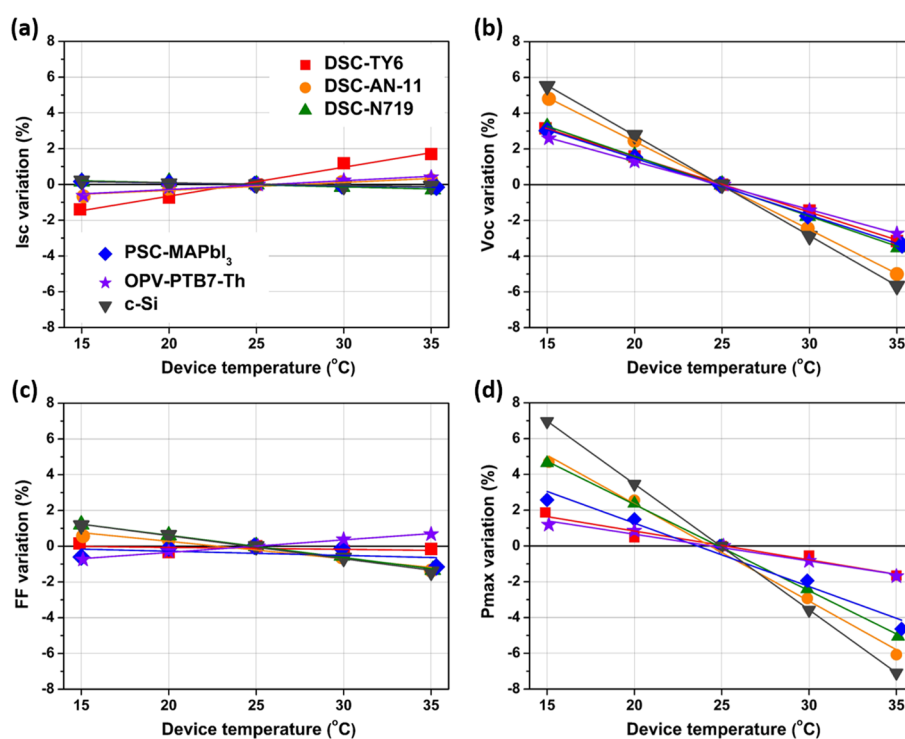
**FIGURE 3** Current density-voltage (J - V) curves of devices (25 ± 1 °C) under CFL and LED with an absolute illuminance of 1000 lx at $\theta = 0$ degree. The sampling delay time is 15 s (DSC-TY6), 10 s (DSC-AN-11, DSC-N719 and PSC-MAPbI₃) and 100 ms (OPV-PTB7-Th), respectively. The sweeping direction is the forward mode. [Colour figure can be viewed at wileyonlinelibrary.com]

TABLE 2 Photovoltaic parameters and the expanded measurement uncertainty ($k = 2$) of devices (25 ± 1 °C) under CFL and LED light (1000 lx)

Device	Light	J_{sc} ($\mu A\ cm^{-2}$)	V_{oc} (V)	FF (%)	MPD ($\mu W\ cm^{-2}$)	PCE (%)
DSC-TY6	CFL	89.51 ± 1.76	0.769 ± 0.006	78.04 ± 1.64	53.72 ± 1.20	16.5 ± 0.4
	LED	84.96 ± 1.74	0.766 ± 0.006	78.47 ± 1.71	51.07 ± 1.18	15.1 ± 0.4
DSC-AN-11	CFL	44.35 ± 0.77	0.972 ± 0.009	69.31 ± 1.24	29.88 ± 0.55	9.2 ± 0.3
	LED	45.51 ± 0.80	0.977 ± 0.008	70.28 ± 1.28	31.25 ± 0.59	9.2 ± 0.3
DSC-N719	CFL	85.95 ± 1.50	0.681 ± 0.006	76.66 ± 1.46	44.87 ± 0.93	13.8 ± 0.3
	LED	86.24 ± 1.51	0.686 ± 0.006	76.70 ± 1.38	45.38 ± 0.84	13.4 ± 0.3
PSC-MAPbI ₃	CFL	106.8 ± 1.9	0.860 ± 0.007	78.94 ± 1.44	72.50 ± 1.40	22.3 ± 0.5
	LED	112.3 ± 2.0	0.862 ± 0.007	79.07 ± 1.42	76.54 ± 1.41	22.6 ± 0.5
OPV-PTB7-Th	CFL	83.84 ± 1.45	0.693 ± 0.005	66.79 ± 1.17	38.81 ± 0.69	11.9 ± 0.3
	LED	91.75 ± 1.61	0.697 ± 0.005	66.97 ± 1.18	42.83 ± 0.76	12.7 ± 0.3
c-Si	CFL	114.2 ± 1.9	0.438 ± 0.003	69.83 ± 1.18	34.93 ± 0.61	10.7 ± 0.3
	LED	124.3 ± 2.1	0.442 ± 0.003	70.29 ± 1.20	38.62 ± 0.69	11.4 ± 0.3

**FIGURE 4** Temperature dependence of (a) I_{sc} , (b) V_{oc} , (c) FF, and (d) P_{max} for devices under CFL light (ca. 1000 lx at $\theta = 0$ degree). The results are normalized to the values measured at 25 ± 1 °C. [Colour figure can be viewed at wileyonlinelibrary.com]

(see Figure S6b and S6d) does not provide a clear clue to dissect the I_{sc} variation for PSC-MAPbI₃, we speculate that both density of states and charge carriers extraction in the perovskite material should be temperature dependent^{42–48} because the current hysteresis of PSC-MAPbI₃ under the CFL turns to be more serious at higher temperature (Figure S7). A α_{rel} value of ca. $0.05\% \text{ } ^\circ\text{C}^{-1}$ is obtained for OPV-PTB7-Th under the same conditions (Figure 4a, Figure S5a and Table 3). The similar feature of current enhancement measured outdoor or under the simulated sunlight has been reported.^{37–40} The reasons described in the previous studies are the improvement of charge carrier mobility, reduction of bandgap

of the light absorption materials, and the moderation of defects at higher temperature. However, it is found that the R_s of OPV-PTB7-Th under room light (Figure S6b) surprisingly raises a little with temperature, which is contrary to the findings in the earlier works using a solar simulator.^{37,38} Moreover, R_{sh} of OPV-PTB7-Th shows an analogous trend to that of the R_s but the augmenting magnitude is larger (Figure S6d). These results imply that the factor of increasing I_{sc} in OPV-PTB7-Th at higher temperature should be dominated by the accession of charge carrier concentration (due to the shrunk bandgap of light harvesting materials) and the diminished charge recombination.

TABLE 3 Relative temperature coefficients of photovoltaic parameters for devices under CFL and LED light (ca. 1000 lx)^a

Device	Light	$\alpha_{\text{rel}} (\% \text{ } ^\circ\text{C}^{-1})$	$\beta_{\text{rel}} (\% \text{ } ^\circ\text{C}^{-1})$	$\kappa_{\text{rel}} (\% \text{ } ^\circ\text{C}^{-1})$	$\gamma_{\text{rel}} (\% \text{ } ^\circ\text{C}^{-1})$
DSC-TY6	CFL	0.162 (0.013)	-0.312 (0.010)	-0.011 (0.002)	-0.161 (0.029)
	LED	0.061 (0.005)	-0.255 (0.008)	-0.006 (0.001)	-0.197 (0.036)
DSC-AN-11	CFL	0.044 (0.003)	-0.493 (0.018)	-0.097 (0.014)	-0.544 (0.080)
	LED	0.011 (0.001)	-0.462 (0.015)	-0.092 (0.013)	-0.540 (0.082)
DSC-N719	CFL	-0.023 (0.002)	-0.336 (0.012)	-0.124 (0.019)	-0.483 (0.080)
	LED	-0.024 (0.002)	-0.342 (0.012)	-0.100 (0.014)	-0.464 (0.069)
PSC-MAPbI ₃	CFL	-0.015 (0.001)	-0.318 (0.010)	-0.023 (0.003)	-0.354 (0.055)
	LED	-0.021 (0.001)	-0.323 (0.010)	-0.105 (0.015)	-0.447 (0.066)
OPV-PTB7-Th	CFL	0.049 (0.003)	-0.269 (0.008)	0.070 (0.010)	-0.150 (0.021)
	LED	0.057 (0.004)	-0.250 (0.007)	0.079 (0.011)	-0.113 (0.016)
c-Si	CFL	-0.014 (0.001)	-0.560 (0.015)	-0.129 (0.017)	-0.703 (0.098)
	LED	-0.006 (0.001)	-0.564 (0.015)	-0.136 (0.019)	-0.705 (0.101)

^aThe values in parentheses represent the standard deviation.

Under steady-state illumination, V_{oc} of devices theoretically depends on the quasi-Fermi levels (E_{Fn} and E_{Fp} for electrons and holes, respectively).⁴⁹ According to the Shockley diode model applicable to describe the I - V characteristics of emerging PVs,^{33,37,45,49-51} V_{oc} is highly related to the temperature of the device (T), I_{sc} and reverse saturation current (I_0), the relationship among which can be described as Equation (3):

$$V_{\text{oc}} = \frac{E_{\text{Fn}} - E_{\text{Fp}}}{q} = \frac{nK_{\text{B}}T}{q} \ln \left(\frac{I_{\text{sc}}}{I_0} + 1 \right) \quad (3)$$

where q is the elementary charge, n is the diode ideality factor (typically larger than unity for actual PVs), and K_{B} is the Boltzmann constant.

As a general feature, V_{oc} falls upon raising device temperature, due to the fact that high temperature leads the enhancement in I_0 because the energy difference between the quasi-Fermi levels is reduced. In this study, V_{oc} of the emerging PVs under the CFL and LED light decreases at elevated temperature (Figure 4b and Figure S5b), as expected. The relative voltage-temperature coefficients (β_{rel}) provided in Table 3 display clearly that the thermal effects on V_{oc} is more pronounced than that of I_{sc} for all the cells. Compared with the low V_{oc} and negative β_{rel} of c-Si ($-0.56\% \text{ } ^\circ\text{C}^{-1}$), the next-generation PVs (with the β_{rel} in the approximate range of $-0.25\% \text{ } ^\circ\text{C}^{-1} \sim -0.49\% \text{ } ^\circ\text{C}^{-1}$) exhibit prominent merits toward realistic applications. It is noticeable that the β_{rel} value of DSC-AN-11 consisting of two subcells connected in series is more negative than that of the DSC-TY6 and DSC-N719 (ca. $-0.3\% \text{ } ^\circ\text{C}^{-1}$). When V_{oc} of each subcell is taken into consideration, the voltage-dependence of β_{rel} is found to be higher V_{oc} leads higher (less negative) β_{rel} value (Figure S8). These results suggest that the temperature effects on V_{oc} for the DSCs should be predictable according to the simple one-diode model.⁵¹

The temperature dependence of FF is also crucial to the overall performance of device. From the equivalent circuit model, an ideal fill factor (FF_0) of PVs (without R_{s} and R_{sh}) can be represented approximately as Equation (4),⁵² in which v_{oc} is the dimensionless voltage (V_{oc} divided by $nK_{\text{B}}T/q$, wherein n is unity):

$$FF_0 = \frac{v_{\text{oc}} - \ln(v_{\text{oc}} + 0.72)}{v_{\text{oc}} + 1} \quad (4)$$

When both R_{s} and R_{sh} are taken into account for the real PVs, FF can be expressed as Equation (5)⁵⁰:

$$FF = FF_s \left(1 - \frac{v_{\text{oc}} + 0.72}{v_{\text{oc}}} \times \frac{FF_s}{r_{\text{sh}}} \right) \quad (5)$$

in which

$$FF_s = FF_0(1 - 1.1r_s) + \frac{r_s^2}{5.4} \quad (6)$$

and FF_0 is the ideal fill factor defined in Equation (4), FF_s is the fill factor of PVs with R_{s} only, v_{oc} is the normalized open-circuit voltage (V_{oc} divided by $nK_{\text{B}}T/q$, wherein n is larger than unity), r_s and r_{sh} are normalized resistances that the actual resistances (R_{s} and R_{sh}) are divided by $V_{\text{oc}}/I_{\text{sc}}$.

Thus, FF tends to be lower when V_{oc} or R_{sh} declines, accompanied by increase of I_{sc} , R_{s} and n at higher temperature. As found in the three DSC devices and PSC-MAPbI₃ (see Figure 4c, Figure S5c and Table 3), the corresponding relative fill factor-temperature coefficients (κ_{rel}) are negative (in the approximate range of $-0.01\% \text{ } ^\circ\text{C}^{-1} \sim -0.12\% \text{ } ^\circ\text{C}^{-1}$). In general, diagnoses of FF could be merely focused on R_{s} and R_{sh} . Interestingly the three DSCs with liquid electrolytes display that the variation in R_{s} is larger than that in R_{sh} (Figure S6a and S6c), while the trend of R_{s} and R_{sh} for PSC-MAPbI₃ and OPV-PTB7-Th is reversed (Figure S6b and S6d), being found to be $R_{\text{s}} < R_{\text{sh}}$. These results reflect the electron and ion diffusions in the mesoscopic TiO₂ film and electrolyte, respectively, play important roles for FF. In PSC-MAPbI₃ and OPV-PTB7-Th (all solid-state devices), the current leakage from the pinholes in the film or from the thermal-induced traps are dominant. Actually the temperature dependence of R_{s} and R_{sh} is insufficient to clarify definitively the thermal-induced variation in FF. Therefore we estimated the changes in ideality factor (n) according to Equation (5). The n value of the DSCs increases with temperature, which could

offset the decrease in R_s (Figure S6e) and contribute to the reduced FF. On the other hand, as shown in Figure S6f the factor (n) for PSC-MAPbI₃ fluctuates irregularly with temperature, which needs to be addressed in our future studies. In OPV-PTB7-Th, the lower n value at higher temperature not only implies the suppressed charge recombination, but also accounts for the positive κ_{rel} values (ca. 0.08% °C⁻¹). Moreover, it is noted that the reduction of n for OPV-PTB7-Th at elevated temperature contradicts the conclusion in previous study.⁵⁰ The results imply that the insights of thermal-induced variation in cell parameters measured under dim light might be dissimilar to the scenario under simulated sunlight.

The relative power-temperature coefficients (γ_{rel}) extracted from Figure 4d and Figure S5d for the next-generation PV devices all have the minus sign (in the approximate range of -0.11% °C⁻¹ ~ -0.54% °C⁻¹ (Table 3)), depending mainly on the β_{rel} values. Compared with the γ_{rel} of c-Si (ca. -0.70% °C⁻¹), encouragingly the Pmax of these emerging PVs is less-sensitive to temperature, which emphasizes the high potential of the next-generation PVs for indoor applications. The inconsistent temperature coefficients (α_{rel} , β_{rel} , κ_{rel} and γ_{rel}) for each device measured under illumination of the CFL and LED light, respectively, signifies that the spectral distribution of room light sources has impacts on the thermal response of DSCs, PSCs and OPVs.

The angular response of PVs is another key factor toward capturing ambient light energy because the light is usually diffused. The relative variations in PV parameters obtained under various incident angles are displayed in Figure 5 (CFL) and Figure S9 (LED). For all devices Pmax declines significantly with the increasing θ (Figure 5a

and Figure S9a), which is affected mainly by the angular dependence of Isc (Figure 5b and Figure S9b). It is noticeable that OPV-PTB7-Th under oblique incident angles shows the decrease of Isc is more steadily than that of the other cells, which should be attributed to the angular dependence of the EQE.^{53,54} Moreover, the behavior of Isc for the emerging PVs, unlike that of c-Si, approaches a cosine curve (as the yellow lines depicted in Figure 5b and Figure S9b), demonstrating clearly the high capability of the next-generation PVs to convert diffused light into electricity. Furthermore, Figure S10 shows the angular dependence of Isc for the next-generation solar cells and the response of an illuminometer are superimposable to each other. The results confirm that the calibrated illuminance meters are more appropriate than the crystalline silicon solar reference cells to evaluate the performance of PVs under ambient light.

The next-generation PV devices show the mild reduction of Voc upon increasing θ (Figure 5c and Figure S9c), which is similar to the light intensity dependent behavior reported in the previous studies.^{9,11,13,15,17,22} The variation of Voc as a function of Isc (Figure S11) shows a trend of slope ($K_B T/q$)⁵⁵ is in the order of DSC-TY6 < OPV-PTB7-Th < PSC-MAPbI₃ < DSC-N719 < DSC-AN-11 < c-Si (Table S1), independent of the light source (CFL or LED). The results suggest that the charge carriers' recombination in the DSC-TY6 and OPV-PTB7-Th under the diffuse light could be less than that of PSC-MAPbI₃ and c-Si. Figure 5d and Figure S9d clearly indicate that the variation in FF for the emerging PVs, except DSC-AN-11, is almost angularly independent when θ angle is smaller than 60 degrees. The declination of FF in DSC-AN-11 is understandable

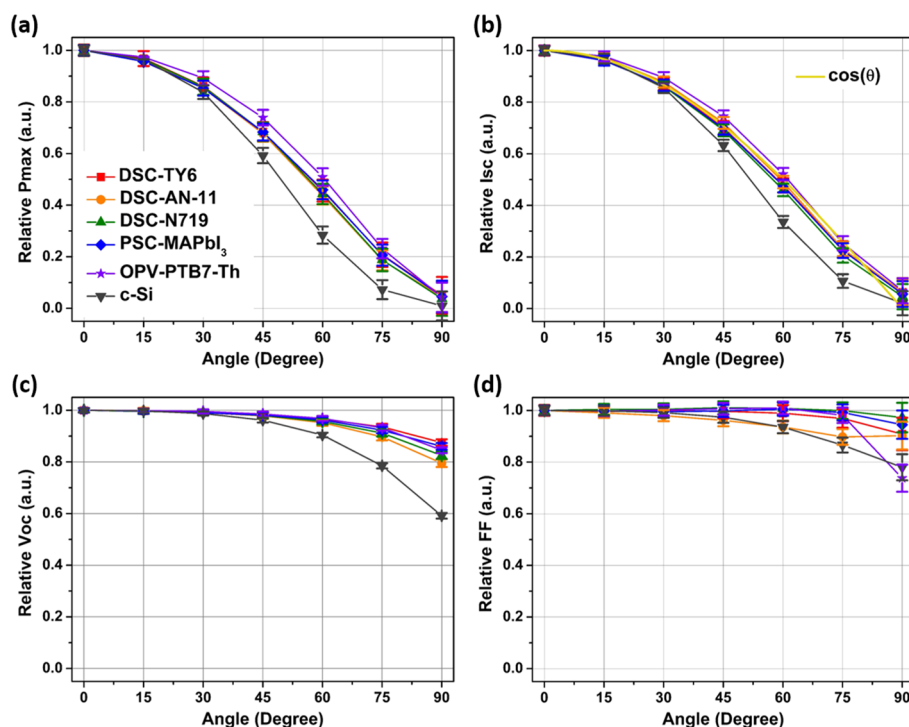


FIGURE 5 Angular dependence of (a) Pmax, (b) Isc, (c) Voc, and (d) FF for devices under CFL light (ca. 1000 lx at θ of 0 degree). The temperature of the devices is 25 ± 1 °C. The results are normalized to the values measured at θ = 0 degree. Error bars represent the standard deviation. [Colour figure can be viewed at wileyonlinelibrary.com]

from the evident recombination behavior mentioned above for Voc. We also found that FF of OPV-PTB7-Th falls steeply at $\theta > 75$ degrees. To gain insights into the changes of FF, the angular dependence of R_s and R_{sh} for the devices was evaluated. As shown in Figure S12, both R_s and R_{sh} of the devices increase significantly at high incident angles (extremely low light intensity). The noticeable R_s augmentation at high incident angle result in the decreased FF (especially for OPV-PTB7-Th). Also these results imply that reducing bulk resistance of materials and/or contact resistance of the interfaces in devices is crucial to the applications under dim and diffused light.

4 | CONCLUSION







In summary the performance of five next-generation PVs with the aperture area over 4 cm^2 was examined under the modern CFL and LED lighting. At the illumination level of 1000 lx and the device temperature at $25 \pm 1^\circ\text{C}$, the emerging PVs display good PCE ranging from 9.2% to 22.6%. In addition to the highest PCE achieved by PSC-MAPbI₃ among all the cells tested, the state-of-the art DSCs and OPV-PTB7-Th exhibit higher Voc (up to approximate 1 V), less thermal dependence of Voc and Pmax ($< -0.55\%^\circ\text{C}^{-1}$; in the temperature range of $15^\circ\text{C} \sim 35^\circ\text{C}$), and broader angular response (over 75 degrees) of the PV parameters than that of conventional single crystalline silicon cells. These results demonstrate the excellent potential of the emerging PVs in harvesting ambient light energy. The thermal and angular dependence of series and shunt resistances is also scrutinized to gain insights into the variations in PV parameters. The protocols of PV performance characterization and data analysis presented in this work not only establish a new platform to reliably rate various PVs for indoor applications, but also guide new directions to advance device optimizations of perovskite, dye-sensitized and organic thin-film photovoltaics.

ACKNOWLEDGEMENTS

We thank Yoshihiro Hishikawa and Sanekazu Igari from the National Institute of Advanced Industrial Science and Technology (AIST), Japan for suggestions, and the Yamashita Denso Corporation (YDC), Japan for discussing the design of indoor lighting systems. The Advanced Laboratory of Accommodation and Research for Organic Photovoltaics (AROPV), the Ministry of Science and Technology (MOST), Taiwan, Republic of China as well as the financial supports from the MOST, Taiwan, Republic of China (Grant no. 106-2731-M-008-003-MY2, 106-2119-M-008-022, 106-2731-M-008-001, 106-2119-M-005-001, 106-2119-M-260-001, 106-2119-M-006-003, 105-2112-M-007-016-MY3, 105-2628-E-007-008-MY3, 105-2119-M-009-008 and 107-2113-M-008-016-MY2), and the Bureau of Energy, Ministry of Economic Affairs, Taiwan, Republic of China are gratefully acknowledged.

ORCID

Chia-Yuan Chen  <https://orcid.org/0000-0002-7935-4076>

Kuan-Min Huang  <https://orcid.org/0000-0001-9444-9201>
 Chen-Yu Yeh  <https://orcid.org/0000-0002-7815-5681>
 Ching-Yao Lin  <https://orcid.org/0000-0002-3963-5244>
 Yuh-Lang Lee  <https://orcid.org/0000-0002-0469-5896>
 Hao-Wu Lin  <https://orcid.org/0000-0003-4216-7995>
 Hsin-Fei Meng  <https://orcid.org/0000-0002-5735-6302>
 Pi-Tai Chou  <https://orcid.org/0000-0002-8925-7747>
 Chun-Guey Wu  <https://orcid.org/0000-0001-8540-5602>

REFERENCES

1. Yin C, Chiu CF, Hsieh CC. A 0.5 V, 14.28-kframes/s, 96.7-dB Smart image sensor with array-level image signal processing for IoT applications. *IEEE T Electron Devices*. 2016;63(3):1134-1140.
2. Bui AK, Xiao ZK, Siek L. Digitally-controlled H-bridge DC-DC converter for micropower PV energy harvesting system. in *IEEE Int Symp on Integrated Circuits IEEE Singapore*. 2016.
3. Liu X, Sánchez-Sinencio E. An 86% efficiency 12 μW self-sustaining PV energy harvesting system with hysteresis regulation and time-domain MPPT for IOT smart nodes. *IEEE J Solid-State Circuits*. 2015;50(6):1424-1437.
4. Hagfeldt A, Boschloo G, Sun L, Kloo L, Pettersson H. Dye-sensitized solar cells. *Chem Rev*. 2010;110(11):6595-6663.
5. Sacco A, Rolle L, Scaltrito L, Tresso E, Pirri CF. Characterization of photovoltaic modules for low-power indoor application. *Appl Energy*. 2013;102:1295-1302.
6. Rossi FD, Pontecorvo T, Brown TM. Characterization of photovoltaic devices for indoor light harvesting and customization of flexible dye solar cells to deliver superior efficiency under artificial lighting. *Appl Energy*. 2015;156:413-422.
7. Li Y, Grabham NJ, Beeby SP, Tudor MJ. The effect of the type of illumination on the energy harvesting performance of solar cells. *Sol Energy*. 2015;111:21-29.
8. Wang CL, Lin PT, Wang YF, et al. Cost-effective anthryl dyes for dye-sensitized cells under one sun and dim light. *J Phys Chem C*. 2015;119(43):24282-24289.
9. Liu YC, Chou HH, Ho FY, et al. A feasible scalable porphyrin dye for dye-sensitized solar cells under one sun and dim light environments. *J Mater Chem A*. 2016;4(30):11878-11887.
10. Freitag M, Teuscher J, Saygili Y, et al. Dye-sensitized solar cells for efficient power generation under ambient lighting. *Nat Photon*. 2017;11:372-378.
11. Tingare YS, Vinh NS, Chou HH, et al. New acetylene-bridged 9,10-conjugated anthracene sensitizers: application in outdoor and indoor dye-sensitized solar cells. *Adv Energy Mater*. 2017;7(18):1700032-1, 1700032-10.
12. Chou HH, Liu YC, Fang G, Cao QK, Wei TC, Yeh CY. Structurally simple and easily accessible perylenes for dye-sensitized solar cells applicable to both 1 sun and dim-light environments. *ACS Appl Mater Interfaces*. 2017;9(43):37786-37796.
13. Tsai MC, Wang CL, Chang CW, et al. A large, ultra-black, efficient and cost-effective dye-sensitized solar module approaching 12% overall efficiency under 1000 lux indoor light. *J Mater Chem A*. 2018;6(5):1995-2003.
14. Lu L, Zheng T, Wu Q, Schneider AM, Zhao D, Yu L. Recent advances in bulk heterojunction polymer solar cells. *Chem Rev*. 2015;115(23):12666-12731.
15. Steim R, Ameri T, Schilinsky P, et al. Organic photovoltaics for low light applications. *Sol Energy Mater Sol Cells*. 2011;95(12):3256-3261.

16. Mori S, Gotanda T, Nakano Y, Saito M, Todoroki K, Hosoya M. Investigation of the organic solar cell characteristics for indoor LED light. *Jpn J Appl Phys*. 2015;54(7):071602-1, 071602-6.
17. Lee HKH, Li Z, Durrant JR, Tsoi WC. Is Organic Photovoltaics Promising for Indoor Applications? *Appl Phys Lett*. 2016;108(25):253301-1, 253301-5.
18. Lechêne BP, Cowell M, Pierre A, Evans JW, Wright PK, Arias AC. Organic solar cells and fully printed super-capacitors optimized for indoor light energy harvesting. *Nano Energy*. 2016;26:631-640.
19. Cutting CL, Bag M, Venkataraman D. Indoor light recycling: a new home for organic photovoltaics. *J Mater Chem C*. 2016;4(43):10367-10370.
20. Aoki Y. Photovoltaic performance of organic photovoltaics for indoor energy harvester. *Org Electron*. 2017;48:194-197.
21. Giacomo FD, Fakhruddin A, Jose R, Brown TM. Progress, challenges and perspectives in flexible perovskite solar cells. *Energ Environ Sci*. 2016;9(10):3007-3035.
22. Chen CY, Chang JH, Chiang KM, Lin HL, Hsiao SY, Lin HW. Perovskite photovoltaics for dim-light applications. *Adv Funct Mater*. 2015;25(45):7064-7070.
23. Giacomo FD, Zardetto V, Lucarelli G, et al. Mesoporous perovskite solar cells and the role of nanoscale compact layers for remarkable all-round high efficiency under both indoor and outdoor illumination. *Nano Energy*. 2016;30:460-469.
24. Dagar J, Castro-Hermosa S, Lucarelli G, Cacialli F, Brown TM. Highly efficient perovskite solar cells for light harvesting under indoor illumination via solution processed SnO₂/MgO composite electron transport layers. *Nano Energy*. 2018;49:290-299.
25. Liu IP, Hung WN, Teng H, Venkatesan S, Lin JC, Lee YL. High-performance printable electrolytes for dye-sensitized solar cells. *J Mater Chem A*. 2017;5(19):9190-9197.
26. Chen CY, Lee WH, Hsiao SY, et al. Vacuum-deposited perovskite photovoltaics for highly efficient environmental light energy harvesting. *J Mater Chem A*. 2019;7(8):3612-3617.
27. Tsai PT, Lin KC, Wu CY, et al. Towards long-term stable and efficient large-area organic solar cells. *ChemSusChem*. 2017;10(13):2778-2787.
28. Chen CY, Ahn SK, Aoki D, et al. International round-robin inter-comparison of dye-sensitized and crystalline silicon solar cells. *J Power Sources*. 2017;340:309-318.
29. Chen CY, Jian ZH, Huang SH, et al. Performance characterization of dye-sensitized photovoltaics under indoor lighting. *J Phys Chem Lett*. 2017;8(8):1824-1830.
30. CIE Standard Illuminants for Colorimetry, CIE S 014-2: 2006.
31. Cojocaru L, Uchida S, Tamaki K, et al. Determination of unique power conversion efficiency of solar cell showing hysteresis in the IV curve under various light intensities. *Sci Rep*. 2017;7:11790-1, 11790-8.
32. Lobato K, Peter LM. Direct measurement of the temperature coefficient of the electron quasi-Fermi level in dye-sensitized nanocrystalline solar cells using a titanium sensor electrode. *J Phys Chem B*. 2006;110(43):21920-21923.
33. Snaith HJ, Schmidt-Mende L, Grätzel M, Chiesa M. Light intensity, temperature, and thickness dependence of the open-circuit voltage in solid-state dye-sensitized solar cells. *Phys Rev B*. 2006;74(4):045306-1, 045306-6.
34. Usami A, Seki S, Mita Y, Kobayashi H, Miyashiro H, Terada N. Temperature dependence of open-circuit voltage in dye-sensitized solar cells. *Sol Energy Mater Sol Cells*. 2009;93(6-7):840-842.
35. Raga SR, Fabregat-Santiago F. Temperature effects in dye-sensitized solar cells. *Phys Chem Chem Phys*. 2013;15(7):2328-2336.
36. Macaira J, Mesquita I, Andrade L, Mendes A. Role of temperature in the recombination reaction on dye-sensitized solar cells. *Phys Chem Chem Phys*. 2015;17(35):22699-22710.
37. Katz EA, Faiman D, Tuladhar SM, et al. Temperature dependence for the photovoltaic device parameters of polymer-fullerene solar cells under operating conditions. *J Appl Phys*. 2001;90(10):5343-5350.
38. Riedel I, Parisi J, Dyakonov V, Lutsen L, Vanderzande D, Hummelen JC. Effect of temperature and illumination on the electrical characteristics of polymer-fullerene bulk-heterojunction solar cells. *Adv Funct Mater*. 2004;14(1):38-44.
39. Thakur AK, Wantz G, Garcia-Belmonte G, Bisquert J, Hirsch L. Temperature dependence of open-circuit voltage and recombination processes in polymer-fullerene based solar cells. *Sol Energy Mater Sol Cells*. 2011;95(8):2131-2135.
40. Tvingstedt K, Deibel C. Temperature dependence of ideality factors in organic solar cells and the relation to radiative efficiency. *Adv Energy Mater*. 2016;6(9):1502230-1, 1502230-13.
41. Wehrenfennig C, Liu M, Snaith HJ, Johnston MB, Herz LM. Charge carrier recombination channels in the low-temperature phase of organic-inorganic lead halide perovskite thin films. *APL Mater*. 2014;2(8):081513-1, 081513-10.
42. Bryant D, Wheeler S, O'Regan BC, et al. Observable hysteresis at low temperature in "hysteresis free" organic-inorganic lead halide perovskite solar cells. *J Phys Chem Lett*. 2015;6(16):3190-3194.
43. Cojocaru L, Uchida S, Sanehira Y, et al. Temperature effects on the photovoltaic performance of planar structure perovskite solar cells. *Chem Lett*. 2015;44(11):1557-1559.
44. Foley BJ, Marlowe DL, Sun K, et al. Temperature dependent energy levels of methylammonium lead iodide perovskite. *Appl Phys Lett*. 2015;106(24):243904-1, 243904-5.
45. Zhang H, Qiao X, Shen Y, Wang M. Effect of temperature on the efficiency of organometallic perovskite solar cells. *J Energy Chem*. 2015;24(6):729-735.
46. Ono LK, Raga SR, Wang S, Kato Y, Qi Y. Temperature-dependent hysteresis effects in perovskite-based solar cells. *J Mater Chem A*. 2015;3(17):9074-9080.
47. Yu H, Lu H, Xie F, Zhou S, Zhao N. Native defect-induced hysteresis behavior in organolead iodide perovskite solar cells. *Adv Funct Mater*. 2016;26(9):1411-1419.
48. Shao S, Liu J, Fang HH, et al. Efficient perovskite solar cells over a broad temperature window: the role of the charge carrier extraction. *Adv Energy Mater*. 2017;7(22):1701305-1, 1701305-10.
49. Nayak PK, Garcia-Belmonte G, Kahn A, Bisquert J, Cahen D. Photovoltaic efficiency limits and material disorder. *Energ Environ Sci*. 2012;5(3):6022-6039.
50. Qi B, Wang J. Fill factor in organic solar cells. *Phys Chem Chem Phys*. 2013;15(23):8972-8982.
51. Hishikawa Y, Doi T, Higa M, et al. Voltage-dependent temperature coefficient of the I-V curves of crystalline silicon photovoltaic modules. *IEEE J Photovolt*. 2018;8(1):48-53.
52. Green MA. Solar cell fill factors: general graph and empirical expressions. *Solid-State Electron*. 1981;24(8):788-789.
53. Dennler G, Forberich K, Scharber MC, Brabec CJ. Angle dependence of external and internal quantum efficiencies in bulk-heterojunction organic solar cells. *J Appl Phys B*. 2007;102(5):054516-1, 054516-7.
54. Mescher J, Mertens A, Egel A, Kettlitz SW, Lemmer U, Colmann A. Illumination angle and layer thickness influence on the photo current generation in organic solar cells: a combined simulative and experimental study. *AIP Adv*. 2015;5(7):077188-1, 077188-6.

55. Proctor CM, Nguyen TQ. Effect of leakage current and shunt resistance on the light intensity dependence of organic solar cells. *Appl Phys Lett*. 2015;106(8):083301-1, 083301-4.

SUPPORTING INFORMATION

Additional supporting information may be found online in the Supporting Information section at the end of the article.

How to cite this article: Chen C-Y, Kuo T-Y, Huang C-W, et al. Thermal and angular dependence of next-generation photovoltaics under indoor lighting. *Prog Photovolt Res Appl*. 2019;1-11. <https://doi.org/10.1002/pip.3211>